scientific reports

Check for updates

OPEN

Interface identification in micro-LED repair applications via depth profiling using femtosecond laser-induced breakdown spectroscopy

Woonkyeong Jung[1,2,7], Janghee Choi[1,7], Gookseon Jeon[1,3], NaYoon Kim[1,6], Jeongcheol An[4], Inseok Jang[4], Sungho Jeong[4], Young-Joo Kim[2✉] & Hohyun Keum[1,5✉]

The commercialization of micro light-emitting diode (micro-LED) display technology depends on the efficient transfer of millions of individual micro-LEDs onto display panels with high spatial precision and yield. However, the extremely high pixel density in 4 K and 8 K displays poses a significant challenge for defect-free transfer. To maintain display quality and ensure production viability, it is crucial to develop effective strategies for repairing defective chips. While conventional laser-based repair methods have been widely used, they often fall short due to the lack of real-time monitoring capability, making it difficult to precisely control ablation depth without causing unintended damage to adjacent structures. In this study, femtosecond laser-induced breakdown spectroscopy (fs-LIBS) is proposed as a repair tool, offering simultaneous real-time elemental analysis and high spatial resolution. Custom-fabricated micro-LEDs with multilayer structures were analyzed using fs-LIBS under varying laser pulse energies. Spectral emissions from key constituent elements were successfully detected, and variations in Ga and Au signals enabled identification of the interface between the p-pad and p-contact layers. Depth profiling further confirmed this interface by monitoring normalized intensities of Ga and Au signals during consecutive laser pulses. These results were validated by elemental mapping of the ablation craters using scanning electron microscopy with coupled energy dispersive X-ray spectroscopy (SEM-EDS). This study highlights the potential of fs-LIBS as an effective technique for monitoring micro-LED repair, reducing the risk of peripheral damage, and improving repair precision in micro-LED displays.

Keywords Micro-LED repair, Femtosecond laser, Laser-induced breakdown spectroscopy, Depth profiling, Interface identification

Light-emitting diodes (LEDs) convert electrical energy into light through electroluminescence, offering high luminous efficiency and low power consumption, which has enabled their widespread adoption in lighting[1], biosensing[2], signage[3], and displays[4]. Among these, micro-LEDs—typically a few micrometers in all dimensions—are considered a promising next-generation light source for portable electronics, augmented and virtual reality (AR/VR) systems, and unconventional display form factors such as flexible, stretchable, and transparent devices. Their self-emissive nature, high energy efficiency, short response time, broad color gamut, and scalability make them well-suited for advanced display applications. However, large-scale commercialization requires overcoming persistent challenges in high-yield heterogeneous material integration.

[1]Industrial Transformation Technology Department , Research Institute of Sustainable Development Technology Korea Institute of Industrial Technology , 89 Yangdaegiro-gil, Ipjang-myeon, Seobuk-gu, Chungcheongnam-do 31056, Cheonan-Si, Republic of Korea. [2]Department of Mechanical Engineering , Yonsei University , 50 Yonsei-ro, Seodaemun-gu, 03722 Seoul, Republic of Korea. [3]Department of Physics , Yonsei University , 50 Yonsei-ro, Seodaemun-gu, 03722 Seoul, Republic of Korea. [4]School of Mechanical and Robotics Engineering , Gwangju Institute of Science and Technology , 123 Chemdangwagi-Ro, Buk-Gu, 61005 Gwangju, Republic of Korea. [5]Department of Mechanical Engineering , Chung-Ang University , 84 Haekseok-ro, Dongjak-gu, 06974 Seoul, Republic of Korea. [6]Department of Robotics and Mechatronics Engineering, Daegu Gyeongbuk Institute of Science and Technology, 42988 Daegu, Republic of Korea. [7]Woonkyeong Jung and Janghee Choi contributed equally to this work. ✉email: yjkim40@yonsei.ac.kr; hkeum@kitech.re.kr

Micro-LED fabrication processes are largely adapted from semiconductor manufacturing, with III–V compound LEDs grown on sapphire or silicon (Si) wafers. Sapphire remains the preferred substrate due to its low dislocation density and superior crystalline quality for gallium nitride (GaN) epitaxy, while Si wafers offer significant cost advantages and compatibility with conventional Si-based integrated circuits. For full-color, high-resolution displays, processed micro-LED chips must be separated from their growth substrate and transferred onto spatially distinct display panels in large quantities.

Several mass transfer strategies have been developed, including laser-based[5], electrostatic[6], fluidic self-assembly[7,8], elastomer stamp[9,10], and roll-to-roll[11–13] methods. These techniques aim to achieve high spatial precision, transfer yield, and throughput. Nonetheless, high-end 4 K displays contain 3840 × 2160 pixels—over 22 million RGB subpixels—making defective pixels inevitable, even when applying advanced six sigma (6σ) methodologies with state-of-the-art automation. In consumer electronics, defective pixels are unacceptable, necessitating effective repair strategies. Miniaturization exacerbates this challenge, as direct removal and replacement of defective LEDs becomes impractical[14], creating a significant bottleneck in commercialization.

Conventional repair approaches often employ redundant designs, in which redundant pixels are incorporated to replace defective pixels after defects are detected[15]. While this method can be effective, it reduces pixel density, increases circuit complexity, and raises production costs. To achieve ultra-high pixel densities, repair methods that avoid redundancy are essential. Laser-based repair techniques have attracted considerable interest due to their non-contact nature, relatively low cost, and high controllability of processing parameters such as energy, spot size, penetration depth, and scanning speed[15,16]. These methods typically involve laser ablation to selectively remove defective chips, for example by eliminating anisotropic conductive films (ACFs) that connect chips to TFT electrodes[17–19]. A key limitation, however, lies in avoiding peripheral damages to neighboring electrodes, transistors, and circuits, which are located in close proximity in micro-LED displays. Electrode damage can impair electrical contact, rendering pixels non-functional[20,21]. This makes real-time, depth-resolved monitoring during the repair process critical for accurate targeting and minimal peripheral damage.

Laser-induced breakdown spectroscopy (LIBS) presents a promising approach to address this need. LIBS is an atomic emission spectroscopy technique in which a focused laser pulse generates high-temperature plasma at the sample surface[22]. The resulting plasma emission lines, characteristic of the material's elemental composition, enable both qualitative and quantitative analysis[23,24]. LIBS requires no sample pretreatment, can be performed under ambient conditions, and offers real-time, in-situ analysis, making it attractive for applications such as welding monitoring[25], trace element detection[26,27], and depth profiling[28]. Unlike conventional techniques, LIBS can be integrated directly into the repair process, allowing simultaneous material removal and elemental identification. Depth profiling with LIBS involves applying successive laser pulses to a single location, with each pulse ablating a thin layer of material. Plasma emission from each pulse is recorded, and the intensity of element-specific spectral lines is plotted against pulse number, revealing the layer-by-layer composition[29]. This capability has been demonstrated for multilayer materials[30–32] and could enable precise identification of material interfaces in micro-LED repair.

In this study, a femtosecond laser was selected for LIBS due to its ultra-short pulse duration, which minimizes thermal effects and reduces the heat-affected zone (HAZ)[33,34]. Femtosecond pulses lower the ablation threshold, allowing the removal of extremely small volumes per pulse, enabling high-resolution, depth-resolved elemental analysis. Micro-LED devices, typically < 5 μm thick, consist of metallic electrodes (Au, Pt, Al) and RGB emission layers made from GaAs, GaAsP, and AlGaP. For such ultra-thin multilayers, femtosecond LIBS (fs-LIBS) provides the precision necessary for selective ablation without damaging surrounding features. Preliminary experiments were conducted on custom-fabricated micro-LEDs to assess the feasibility of fs-LIBS for real-time monitoring in micro-LED repair. LIBS-based depth composition analysis was applied to identify material interfaces, enabling the selective targeting of defective pixels while minimizing peripheral damage. To the best of our knowledge, this represents the first reported use of LIBS as an in-process monitoring technique for LED repair, underscoring its novelty and its potential to overcome one of the primary bottlenecks in micro-LED defect management.

Experimental details

The schematic of the fs-LIBS setup used in this study is presented in Fig. 1. Plasma was generated using a diode-pumped ytterbium femtosecond laser (s-Pulse HP; Amplitude systems) operated at its third harmonic (λ = 343 nm) with a pulse duration of 550 fs and a repetition rate of 1 Hz. To enhance material absorption and depth resolution, the third harmonic of the femtosecond laser (343 nm) was selected. The micro-LED used in this experiment was coated with a carbon-based layer, which was nearly transparent in the visible to NIR range. UV wavelengths are known to be more strongly absorbed by such transparent materials, enabling more efficient plasma formation and ablation[35]. In contrast, longer wavelengths such as 1030 nm tend to pass through the transparent surface with minimal interaction. A 20 × objective lens (NA = 0.39, LMU-20 × -UVB) was used to focus the laser beam on the sample surface, with a spot size of approximately 2.25 μm. The generated plasma emission was focused into an optical fiber through a dichroic mirror and a plano-convex lens (focal length = 50 mm). A spectrometer equipped with an intensified charge-coupled device (ICCD; PI-MAX3, Princeton Instruments, USA) as a detector was employed to capture plasma emission, using a 2400 grooves/mm grating and a gain of 10. The gate width of the ICCD was set to 1 μs, without any gate delay. The detection of key elements in the LED sample, including carbon (C), gold (Au), and gallium (Ga), was achieved by acquiring wavelength ranges of 220–280 nm, and 270–330 nm. Spectra were collected by applying 10 laser pulses at each energy to a single point, starting from the p-pad region. The laser pulse energy was set to 0.3, 0.5, 0.7, and 0.9 μJ, corresponding to laser fluences of 15.09, 25.15, 35.21, and 45.27 J/cm^2, respectively.

The micro-LED samples used in this study were fabricated with a multilayer heterostructure design. As presented in Table 1, the custom-fabricated micro-LEDs were sequentially deposited in the order listed, following the typical architecture of micro-LEDs. To enhance surface stability and minimize contamination, the
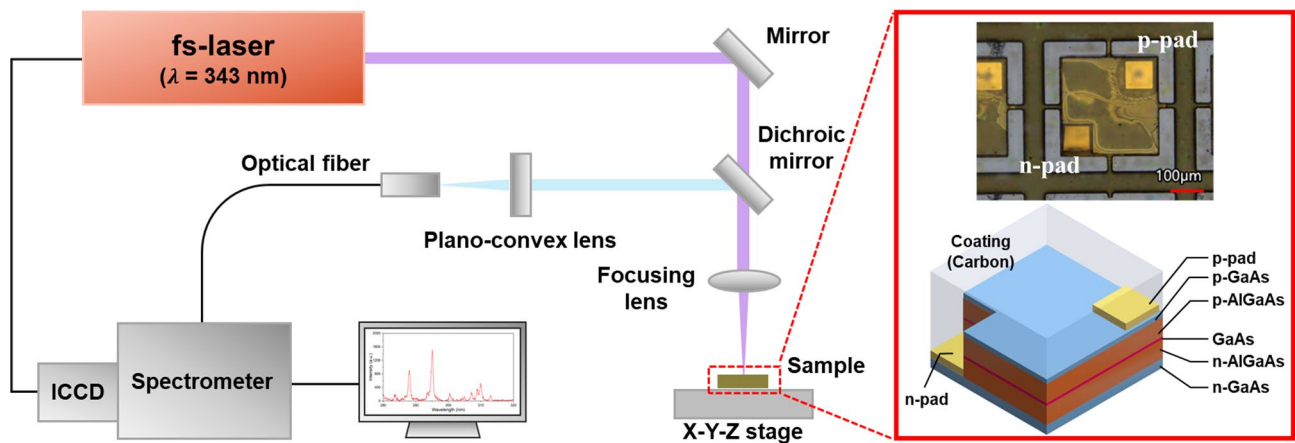
Fig. 1. Schematic of the fs-LIBS system for micro-LED analysis.

Layer	Composition	Thickness (μm)	Dopant	Doping (cm^{-3})
p-pad	Pt/Ti/Pt/Au	0.14	-	-
p-contact	GaAs	0.05	Zn	1.00E+19
p-spreader	Al$_{0.45}$GaAs	0.8	Zn	1.00E+19
p-cladding	Al$_{0.33}$GaAs	0.2	Zn	5.00E+17
Active region	GaAs	0.01	-	-
n-cladding	Al$_{0.33}$GaAs	0.2	Si	1.00E+18
n-spreader	Al$_{0.45}$GaAs	0.8	Si	1.00E+18
n-contact	GaAs	0.5	Si	5.00E+18
Sacrificial	Al$_{0.95}$GaAs	0.5	-	-

Table 1. Layer composition, thickness, and doping specifications of custom-fabricated micro-LEDs.

fabricated micro-LEDs were coated with a thin layer of carbon. Additionally, the sacrificial layer was included but was not used in the actual experiments because the sacrificial layer was removed before proceeding with the experiments. The micro-LEDs were fabricated with micro-scale dimensions to align with the application requirements of micro-LED display repair. The final fabricated micro-LED chips had an area of 280 $\times$ 280 μm, with a total thickness of 2.72 μm. Contact pads were designed with an area of 80 $\times$ 80 μm and had a thickness of 0.14 μm.

Results and discussion
Spectroscopic analysis
In general, LIBS spectra exhibit background emission, primarily originating from continuum radiation due to bremsstrahlung, which occurs when electrons are decelerated by the electric field during collisions[36]. Therefore, applying an appropriate gate delay is critical for suppressing background emission and acquiring spectra with high signal-to-background (SBR) and signal-to-noise ratios (SNR)[37,38]. However, in this study, no gate delay was applied. This decision was based on the specific characteristics of the femtosecond laser, which generated low background emission due to reduced plasma temperature resulting from minimal laser-plasma interaction[33]. In addition, the use of low pulse energy (0.3–0.9 μJ) in our experiments generated a highly localized plasma that cooled rapidly and produced minimal continuum emission[39,40]. To prioritize capturing the emitted light from the early stage of plasma evolution for interface identification, rather than achieving the highest possible SBR and SNR, we collected the entire spectral emission without temporal gating. The residual background emission was subsequently removed using baseline estimation and denoising using sparsity (BEADS)[41]. This method assumes that an observed spectrum consists of sparse characteristic peaks, a baseline, and Gaussian noise-an assumption that corresponds well with the typical structure of LIBS signals.

In this experiment, simultaneous detection of Ga and Au emissions was essential for distinguishing the LED and electrode layers. Both signals were successfully observed within the wavelength range of 280–320 nm. Figure 2 shows the averaged LIBS spectra from three repeated experiments performed with various laser pulse energies (0.3, 0.5, 0.7, and 0.9 μJ) at different points on the p-pad. These spectra represent the results of the first to fifth laser pulses out of 10 consecutive laser pulses. The initial pulse produced a spectrum with notably higher noise levels than those obtained in subsequent measurements, due to the highly reflective surface of the polished coating layer, which reduces the absorption of laser energy[42]. No emission line was detected at the second laser pulse, likely because the laser interacted with a carbon-based coating layer whose emission lines
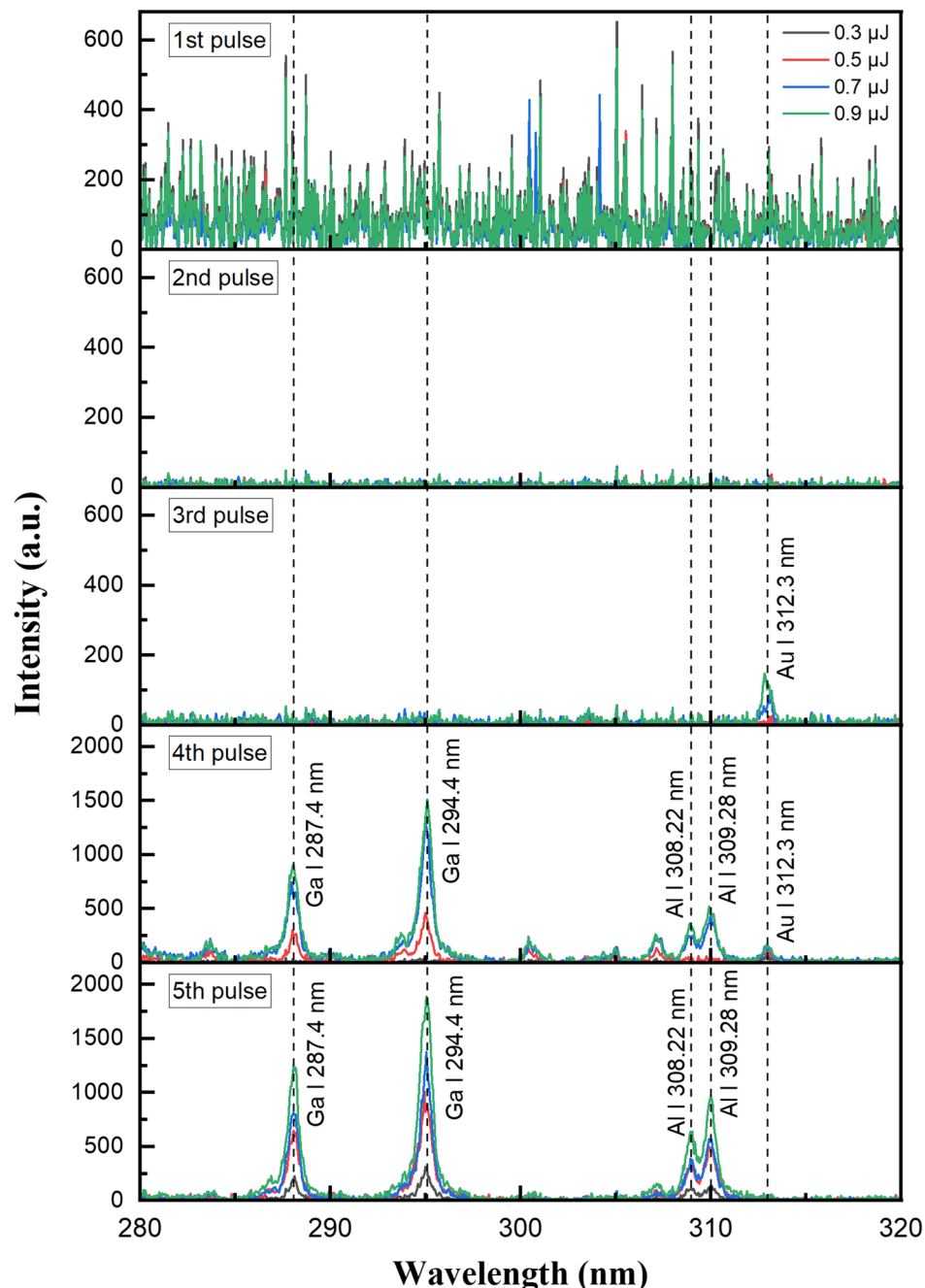
Fig. 2. LIBS spectra of the micro-LED at different laser energies (0.3, 0.5, 0.7, and 0.9 μ J).

fall outside the analyzed wavelength range. In contrast, the Au (I) 312.3 nm line was observed at the third laser pulse, indicating that the coating layer was removed during the first two pulses, thereby exposing the underlying electrode material. In the fourth laser pulse, emission lines of Ga (I) line at 287.4 nm and 294.42 nm, Al (I) line at 308.22 nm and 309.28 nm, and Au (I) line at 312.3 nm were detected. Notably, the simultaneous detection of Au and Ga in the fourth laser pulse suggests that the interface between the p-pad and p-contact layer corresponds between the third and fourth pulses. At the fifth laser pulse, Ga and Al signals were still observed, whereas the Au signal was no longer detected, indicating that the thin Au layer had been ablated under all laser energy conditions. These spectral results match well with the known elemental composition of the micro-LED sample, demonstrating that LIBS is a suitable technique for ultra-thin micro-LED structures.

To apply the LIBS technique for monitoring the micro-LED repair process, it is necessary to identify the interfaces by analyzing the extremely thin layers of the LED. Typically, the laser-material interaction varies with pulse energy, and as the laser energy increases, the ablated mass increases, thereby enhancing the LIBS signal intensity[43]. However, in the case of micro-LED depth profiling, a low average ablation rate (AAR) is also a critical factor along with signal intensity, since an excessively low AAR can result in poor signal intensity, thereby

Pulse energy (μJ)	SNR of Ga (I) 294.4 nm line	SNR of Au (I) 312.3 nm line
0.3	31.12	8.64
0.5	51.47	11.36
0.7	98.20	11.50
0.9	125.83	13.36

Table 2. SNR values of Ga and Au lines at different laser pulse energies, calculated from the 4th laser pulse.
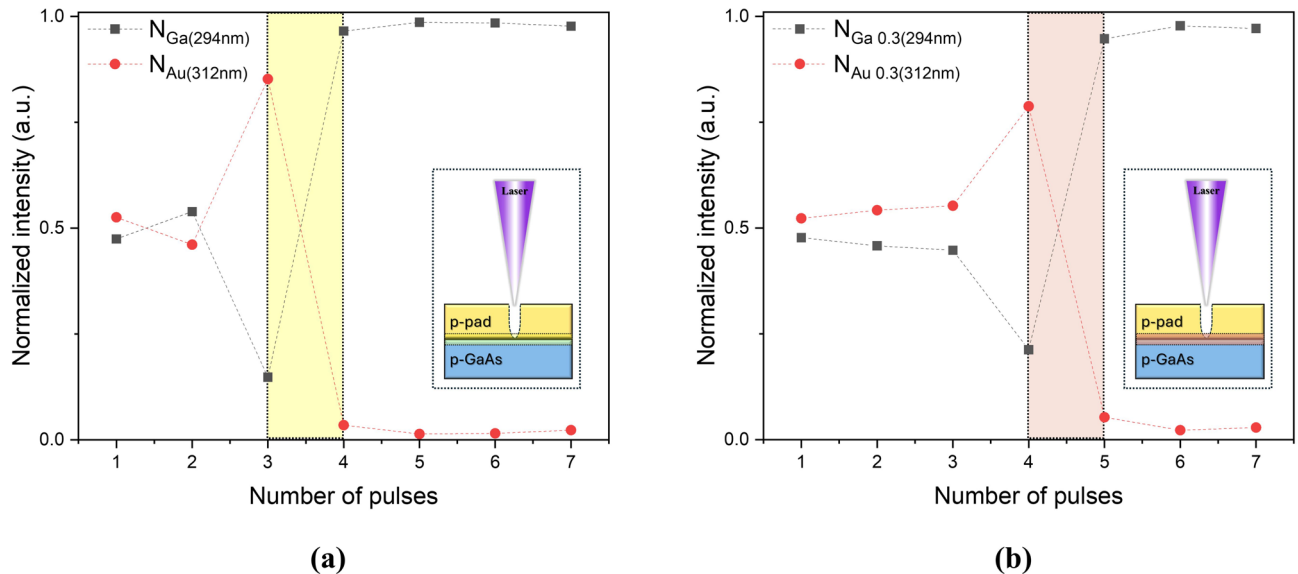

(a)

(b)

Fig. 3. Variations of the normalized line intensities of Ga (I) 294.4 nm and Au (I) 312.3 nm as a function of the number of laser pulses at (a) 0.7 μJ and (b) 0.3 μJ.

hindering both detection sensitivity and profiling accuracy. Consequently, given that the thickness of the p-pad is only 0.14 μm, it is necessary to select an appropriate laser energy condition that ensures a low AAR and sufficient signal intensity to enhance the SNR. Table 2 shows the SNR values calculated at the fourth laser pulse. The Ga (I) 294.4 nm and Au (I) 312.3 nm lines were selected as characteristic emission lines. In general, an SNR value greater than 3 (SNR > 3) is considered sufficient to distinguish signal from noise[44]. However, depending on the experimental objective and noise environment, higher SNR thresholds may be applied to ensure greater data reliability[45]. Although lower laser pulse energy is advantageous for the depth-wise analysis of micro-LED, the SNR values at 0.3 and 0.5 μJ were significantly lower compared to those at 0.7 and 0.9 μJ. At 0.7 μJ, scanning electron microscopy (SEM; Su8230, Hitachi) and optical microscopy (Supplementary Fig. 1) revealed highly localized ablation with no detectable damage to the surrounding regions. Thus, in this experiment, 0.7 μJ was selected for further investigation.

Depth profiling

For accurate depth profiling, fluctuations in the laser beam, variations in the working distance, and differences in sample properties-which can lead to variability in the LIBS signal-should be corrected. In general, normalization is commonly used to reduce such signal variations. In this experiment, the normalized intensities N_{Ga} and N_{Au} were calculated as follows:

$$N_{Ga} = \frac{I_{Ga}}{I_{Au}+I_{Ga}} \text{ and } N_{Au} = \frac{I_{Au}}{I_{Au}+I_{Ga}} \tag{1}$$

Where I_{Au} is the integrated intensity of Au (I) emission line at 312.2 nm, and I_{Ga} is that of Ga (I) emission line at 294.4 nm. This normalization method is commonly used in LIBS depth profiling, as it enhances the layer-by-layer distinction by enabling a relative evaluation of each signal.

Since the purpose of this study is to investigate the potential of real-time monitoring during the micro-LED repair process using LIBS, it is crucial to interpret spectral variations based on a single measurement rather than statistical averaging. Accordingly, the data presented in Fig. 3a and b represent the spectral variation observed in a single representative experiment. Figure 3a illustrates the variation in the N_{Ga} and N_{Au} as a function of the number of laser pulses at a laser energy of 0.7 μJ. In the first and second laser pulses, the normalized intensities of Ga and Au were both close to 0.5, indicating that the signals had comparable intensity levels. This is because neither signal was detected due to the presence of the coating layer above the p-pad. As the laser pulse

progressed along the depth direction, the normalized Au intensity increased sharply between the second and third laser pulses as the pulse reached the Au-rich p-pad. Thereafter, the decrease in Au intensity between the third and fourth pulses is attributed to the transition into the Ga-containing p-contact layer. In contrast, the normalized Ga intensity exhibited the opposite trend. In the LIBS spectrum (Fig. 2), both Au and Ga emission lines were simultaneously detected at the fourth laser pulse. In Fig. 3, however, the Au appears to be absent at this pulse, which is attributed to the relatively much higher intensity of Ga compared to Au. Although the normalization results do not fully reflect the raw spectral data, the presence of an interface between the third and fourth laser pulses remains evident. Figure 3b shows the depth profiling results obtained at the laser energy of 0.3 μJ. The normalized intensity profiles of Au and Ga show a trend similar to those observed at 0.7 μJ. The normalized intensities of Au and Ga remained close to 0.5 until the interface, after which the Au signal sharply increased and then decreased, whereas the Ga signal showed the opposite trend. As mentioned above, higher laser energy results in deeper ablation. Therefore, at 0.3 μJ, the sharp transition in normalized intensities appears between the fourth and fifth laser pulses. These results indicate that the ablation rate and the number of laser pulses required to reach the interface vary depending on the laser pulse energy, whereas the overall shape of the normalized intensity profiles remains unaffected. From an industrial application perspective, variations in laser energy due to on-site environmental factors are common. Such fluctuations can lead to either deeper or shallower ablation in the depth-wise direction. In this context, LIBS can serve as a useful technique for the real-time detection of interfaces.

The atomic force microscopy (AFM, NX10, Park Systems) analysis was performed to investigate the evolution of the ablation crater depth as a function of the number of laser pulses. The AFM images of ablation craters and their cross-sectional profiles are presented in Supplementary Fig. S2. Crater depth increases with increasing pulses, demonstrating a cumulative material removal process. The measured depths of the craters were 1.244, 2.625, 3.217, and 4.648 μm for 1, 2, 5, and 10 laser pulses, respectively. The ablation rate exhibited a nonlinear trend with the number of pulses. Considering that the ablation depth at the 10th laser pulse was 4.648 μm, while the Rayleigh range in this experimental setup was 8.9 μm, the observed differences in ablation rate can primarily be attributed to the material properties. In general, the ablation rate of carbon is higher than that of Au and GaAs.

Validation of LIBS depth profiling by SEM–EDS

To evaluate the reliability of LIBS spectral data, a comparative analysis was conducted. Morphology and elemental mapping of ablation craters were characterized using a SEM equipped with energy-dispersive X-ray spectroscopy (EDS). Figure 4 presents the results of the EDS elemental mapping performed on samples after 1, 2, 5, and 10 laser pulses at the laser energy of 0.7 μJ. Based on the LIBS spectra in Fig. 2, at the 2nd pulse—which corresponds to the surface condition after a single laser pulse (Fig. 4a)—no emission lines were detected. This indicates that after one laser pulse, the carbon layer still remained, and the underlying Au layer had not yet been reached. The Au signals observed in the EDS data may be attributed to the penetration depth of electrons in EDS measurements[46]. After the second laser pulse (Fig. 4b), Ga and As signals remained undetected, while the Au signal intensity increased, implying that the Au layer began to appear after the second pulse, which is consistent with the LIBS spectra showing the emergence of Au signals at the third laser pulse. Between the third and fifth pulses, Au completely disappears from the spectral results as shown in Fig. 2, whereas Ga and As begin to emerge at the fifth pulse and become increasingly prominent thereafter (Fig. 4c-d). The elemental mapping results are consistent with both the LIBS results and the LED structure. Prior to laser irradiation, the LED surface is covered with a carbon-coated layer. After ablation of this layer, the underlying gold-based p-pad is exposed. Subsequent removal of the p-pad reveals the p-type GaAs layer. Accordingly, Au signals observed in both EDS and LIBS appear during the intermediate stage and then disappear as the gold layer is fully removed. In contrast, Ga signals detected by both techniques persist once the GaAs layer is exposed.

In the Au mapping images shown in Fig. 4c-d, an accumulation of Au at the crater edges is observed. At the relatively high fluence used in this study (35.21 J/cm^2), transient melting and the formation of molten pools can occur. These molten pools can result in resolidified structures and rim morphologies, driven by hydrodynamic instabilities[47]. Additionally, Au possesses a relatively higher density and lower diffusion rate compared to Ga, it tends to redeposit more intensely along the crater periphery[48]. When comparing elemental distribution profiles obtained from EDS with the LIBS spectral data, both analytical methods exhibit consistent trends: the Au concentration decreases, while the Ga concentration increases with an increasing number of laser pulses.

Conclusion

In this study, fs-LIBS was investigated as a real-time monitoring technique for micro-LED repair, with a focus on depth profiling and elemental analysis. The LIBS spectroscopic results successfully detected Au and Ga emission lines, enabling the identification of the interface between the p-pad and p-contact layers. Although all pulse energies enabled the detection of emission lines from the constituent elements of the micro-LED, 0.7 μJ was identified as optimal energy, considering both SNR and minimal material removal. Normalized depth profiles revealed that the interface was distinguishable based on the variations in Ga and Au signal intensities as a function of the laser pulse number, with a clear transition observed between the third and fourth laser pulses. To validate the spectral data, EDS elemental mapping was conducted on ablation craters generated after different numbers of pulses. The EDS images are consistent with the LIBS results. These findings demonstrate that fs-LIBS provides depth-resolved information, enabling precise defect localization and selective material removal, thereby making it a promising technique for real-time process monitoring in micro-LED repair. Compared to conventional defect repair methods, fs-LIBS offers in-situ elemental analysis, which minimizes damage to adjacent components such as electrodes and transistors.
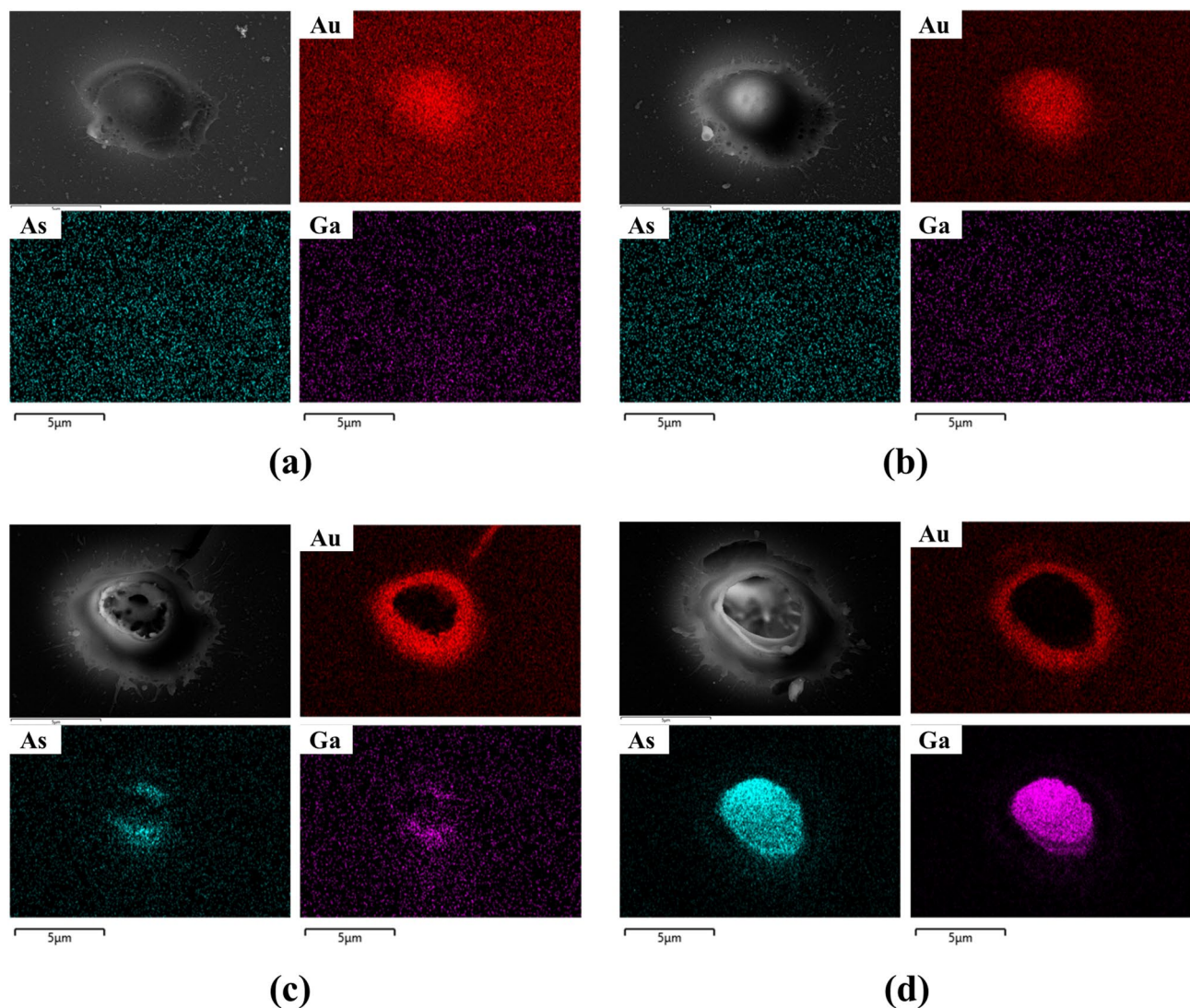
Fig. 4. EDS elemental mapping analysis after (**a**) 1, (**b**) 2, (**c**) 5, and (**d**) 10 laser pulses at a laser pulse energy of 0.7 μ J.

Data availability
The data that support the findings of this study are available from the corresponding author on reasonable request.

References

1. Olle, M. & Viršile, A. The effects of light-emitting diode lighting on greenhouse plant growth and quality. *AFSci* **22**, 223–234 (2013).
2. Bhavsar, K., Ross, D., Prabhu, R. & Pollard, P. LED-controlled tuning of ZnO nanowires' wettability for biosensing applications. *Nano Reviews.* **6**, 26711 (2015).
3. Adhikari, R. C., Beyragh, D. S., Pahlevani, M. & Design Fabrication, and testing of a novel design for flexible Light-Emitting diode signage modules. *J. Electron. Packag.* **143**, 031008 (2021).
4. Mei, W. et al. High-resolution, full-color quantum Dot light-emitting diode display fabricated via photolithography approach. *Nano Res.* **13**, 2485–2491 (2020).
5. Marinov, V. R. 52-4: Laser-Enabled Extremely-High rate technology for μLED assembly. *Symp. Digest Tech. Papers.* **49**, 692–695 (2018).
6. Bibl, A., Higginson, J. A., Hu, H. H. & Law, H. F. S. Method of transferring and bonding an array of micro devices. (2013).
7. Schuele, P. J., Sasaki, K., Ulmer, K. & Lee, J. J. Display with surface mount emissive elements. (2017).
8. Wu, Y., Ma, J., Su, P., Zhang, L. & Xia, B. Full-Color realization of Micro-LED displays. *Nanomaterials* **10**, 2482 (2020).
9. Kim, J. H., Kim, B. C., Lim, D. W. & Shin, B. C. Control of adhesion force for micro LED transfer using a magnetorheological elastomer. *J. Mech. Sci. Technol.* **33**, 5321–5325 (2019).
10. Meitl, M. A. et al. Transfer printing by kinetic control of adhesion to an elastomeric stamp. *Nat. Mater.* **5**, 33–38 (2006).

11. Ahn, S. H. & Guo, L. J. Large-Area Roll-to-Roll and Roll-to-Plate nanoimprint lithography: A step toward High-Throughput application of continuous nanoimprinting. *ACS Nano*. **3**, 2304–2310 (2009).
12. Ding, K., Avrutin, V., Izyumskaya, N., Özgür, Ü. & Morkoç, H. Micro-LEDs, a manufacturability perspective. *Appl. Sci.* **9**, 1206 (2019).
13. Sharma, B. K. et al. Load-Controlled roll transfer of oxide transistors for stretchable electronics. *Adv. Funct. Mater.* **23**, 2024–2032 (2013).
14. Zhu, G., Liu, Y., Ming, R., Shi, F. & Cheng, M. Mass transfer, detection and repair technologies in micro-LED displays. *Sci. China Mater.* **65**, 2128–2153 (2022).
15. Lai, S. et al. Applications of lasers: A promising route toward low-cost fabrication of high-efficiency full-color micro-LED displays. *OES* **2**, 230028–230028 (2023).
16. Huang, Y. W., Gao, X. D., Gao, P. P., Ma, B. & Zhang, Y. X. Laser welding monitoring techniques based on optical diagnosis and artificial intelligence: a review. *Adv. Manuf.* **13**, 337–361 (2025).
17. Choi, K. S. et al. (2021) Simultaneous Transfer and Bonding (SITRAB) Process for Micro-LEDs Using Laser-Assisted Bonding with Compression (LABC) Process and SITRAB Adhesive. in. *IEEE 71st Electronic Components and Technology Conference (ECTC)* 1607–1613 (IEEE, San Diego, CA, USA, 2021). https://doi.org/10.1109/ECTC32696.2021.00255
18. Prevatte, C. et al. (2017) Miniature Heterogeneous Fan-Out Packages for High-Performance, Large-Format Systems. in. *IEEE 67th Electronic Components and Technology Conference (ECTC)* 1098–1106 (IEEE, Orlando, FL, USA, 2017). https://doi.org/10.1109/ECTC.2017.325
19. Choi, J., Cho, K. & Cho, S. H. Ablation morphology and characteristic analysis of anisotropic conductive film (ACF) using femtosecond lasers with NIR, Green, and DUV wavelengths for micro-LED display repair. *Appl. Phys. A*. **130**, 140 (2024).
20. Cok, R. S. et al. Inorganic light-emitting diode displays using micro-transfer printing. *J. Soc. Info Disp.* **25**, 589–609 (2017).
21. Zhang, S. et al. Research progress of Micro-LED display technology. *Crystals* **13**, 1001 (2023).
22. Miziolek, A. W., Palleschi, V. & Schechter, I. (2006) LASER-INDUCED BREAKDOWN SPECTROSCOPY (LIBS): Fundamentals and Applications.
23. Xiu, J. et al. Rapid qualitative and quantitative analysis of elemental composition of Cu(In, Ga)Se$_2$ thin films using laser-induced breakdown spectroscopy. *Appl. Opt.* **58**, 1040 (2019).
24. Pořízka, P. et al. Laser-induced breakdown spectroscopy for in situ qualitative and quantitative analysis of mineral ores. *Spectrochimica Acta Part. B: At. Spectrosc.* **101**, 155–163 (2014).
25. Lednev, V. N. et al. Online and in situ laser-induced breakdown spectroscopy for laser welding monitoring. *Spectrochimica Acta Part. B: At. Spectrosc.* **175**, 106032 (2021).
26. Ma, Q. et al. Multielement simultaneous quantitative analysis of trace elements in stainless steel via full spectrum laser-induced breakdown spectroscopy. *Talanta* **272**, 125745 (2024).
27. Tian, H., Jiao, L. & Dong, D. Rapid determination of trace cadmium in drinking water using laser-induced breakdown spectroscopy coupled with chelating resin enrichment. *Sci. Rep.* **9**, 10443 (2019).
28. Abdelhamid, M., Grassini, S., Angelini, E., Ingo, G. M. & Harith, M. A. Depth profiling of coated metallic artifacts adopting laser-induced breakdown spectrometry. *Spectrochimica Acta Part. B: At. Spectrosc.* **65**, 695–701 (2010).
29. Messaoud Aberkane, S. et al. Depth profiling of alumina thin films using laser induced breakdown spectroscopy: structural and morphological dependence. *Thin Solid Films*. **653**, 293–300 (2018).
30. Lednev, V. N. et al. Elemental profiling of laser cladded multilayer coatings by laser induced breakdown spectroscopy and energy dispersive X-ray spectroscopy. *Appl. Surf. Sci.* **416**, 302–307 (2017).
31. Rabasović, M. S. et al. Evaluation of laser-induced thin-layer removal by using shadowgraphy and laser-induced breakdown spectroscopy. *Appl. Phys. A*. **122**, 186 (2016).
32. Oelmann, J. et al. Depth-resolved sample composition analysis using laser-induced ablation-quadrupole mass spectrometry and laser-induced breakdown spectroscopy. *Spectrochimica Acta Part. B: At. Spectrosc.* **144**, 38–45 (2018).
33. Labutin, T. A., Lednev, V. N., Ilyin, A. A. & Popov, A. M. Femtosecond laser-induced breakdown spectroscopy. *J. Anal. Spectrom.* **31**, 90–118 (2016).
34. LaHaye, N. L., Kurian, J., Diwakar, P. K., Alff, L. & Harilal, S. S. Femtosecond laser ablation-based mass spectrometry: an ideal tool for stoichiometric analysis of thin films. *Sci. Rep.* **5**, 13121 (2015).
35. Barnett, C., Cahoon, E. & Almirall, J. R. Wavelength dependence on the elemental analysis of glass by laser induced breakdown spectroscopy. *Spectrochimica Acta Part. B: At. Spectrosc.* **63**, 1016–1023 (2008).
36. Cremers, D. A. Handbook of Laser-Induced Breakdown Spectroscopy.
37. Borduchi, L. C. L., Milori, D. M. B. P. & Villas-Boas, P. R. Study of the effects of detection times in laser-induced breakdown spectroscopy and missed variation of plasma parameters with gate width. *Spectrochimica Acta Part. B: At. Spectrosc.* **191**, 106409 (2022).
38. Lei, B. et al. Time-resolved characteristics of laser induced breakdown spectroscopy on non-flat samples by single beam splitting. *RSC Adv.* **10**, 39553–39561 (2020).
39. Rieger, G. W., Taschuk, M., Tsui, Y. Y. & Fedosejevs, R. Comparative study of laser-induced plasma emission from microjoule picosecond and nanosecond KrF-laser pulses. *Spectrochimica Acta Part. B: At. Spectrosc.* **58**, 497–510 (2003).
40. Elhassan, A. et al. Nanosecond and femtosecond laser induced breakdown spectroscopic analysis of bronze alloys. *Spectrochimica Acta Part. B: At. Spectrosc.* **63**, 504–511 (2008).
41. Ning, X., Selesnick, I. W. & Duval, L. Chromatogram baseline Estimation and denoising using sparsity (BEADS). *Chemometr. Intell. Lab. Syst.* **139**, 156–167 (2014).
42. Banerjee, S. P. et al. Characterization of organic photovoltaic devices using femtosecond laser induced breakdown spectroscopy. *Appl. Surf. Sci.* **418**, 542–547 (2017).
43. Liu, J. et al. Study of spectral intensity of the laser ablated tungsten plasma and ablation mass at various laser spot sizes and laser fluence in vacuum environment. *Spectrochimica Acta Part. B: At. Spectrosc.* **199**, 106569 (2023).
44. Milán, M. & Laserna, J. J. Diagnostics of silicon plasmas produced by visible nanosecond laser ablation. *Spectrochimica Acta Part. B: At. Spectrosc.* **56**, 275–288 (2001).
45. Šindelářová, A. et al. Methodology for the implementation of internal standard to Laser-Induced breakdown spectroscopy analysis of soft tissues. *Sensors* **21**, 900 (2021).
46. Moro, D., Ulian, G. & Valdrè, G. SEM-EDS nanoanalysis of mineral composite materials: A Monte Carlo approach. *Compos. Struct.* **259**, 113227 (2021).
47. Park, M., Gu, Y., Mao, X., Grigoropoulos, C. P. & Zorba, V. Mechanisms of ultrafast ghz burst Fs laser ablation. *Sci. Adv.* **9**, eadf6397 (2023).
48. Yang, K. et al. Ablation behavior of Ta, tac and Ta/TaC coatings on graphite under high-energy laser irradiation. *J. Mater. Sci.* **59**, 11177–11192 (2024).

Acknowledgements

diagnosis" (KITECH EH-25-0002).

Author contributions

Declarations

Competing interests

The authors declare no competing interests.

Additional information

Supplementary Information The online version contains supplementary material available at https://doi.org/10.1038/s41598-025-24765-3.

Correspondence and requests for materials should be addressed to Y.-J.K. or H.K.

Reprints and permissions information is available at www.nature.com/reprints.

Publisher's note Springer Nature remains neutral with regard to jurisdictional claims in published maps and institutional affiliations.